Multiplicity of morphologies in poly (L-lactide) bioresorbable vascular scaffolds

Artemis Ailianou[a,1], Karthik Ramachandran[a,1], Mary Beth Kossuth[b], James Paul Oberhauser[b], and Julia A. Kornfield[a,2]

[a]Division of Chemistry and Chemical Engineering, California Institute of Technology, Pasadena, CA 91125; and [b]Bioresorbable Vascular Scaffold, Research & Development, Abbott Vascular, Santa Clara, CA 95054

Edited by John A. Rogers, University of Illinois, Urbana, IL, and approved August 12, 2016 (received for review April 22, 2016)

Poly(L-lactide) (PLLA) is the structural material of the first clinically approved bioresorbable vascular scaffold (BVS), a promising alternative to permanent metal stents for treatment of coronary heart disease. BVSs are transient implants that support the occluded artery for 6 mo and are completely resorbed in 2 y. Clinical trials of BVSs report restoration of arterial vasomotion and elimination of serious complications such as late stent thrombosis. It is remarkable that a scaffold made from PLLA, known as a brittle polymer, does not fracture when crimped onto a balloon catheter or during deployment in the artery. We used X-ray microdiffraction to discover how PLLA acquired ductile character and found that the crimping process creates localized regions of extreme anisotropy; PLLA chains in the scaffold change orientation from the hoop direction to the radial direction on micrometer-scale distances. This multiplicity of morphologies in the crimped scaffold works in tandem to enable a low-stress response during deployment, which avoids fracture of the PLLA hoops and leaves them with the strength needed to support the artery. Thus, the transformations of the semicrystalline PLLA microstructure during crimping explain the unexpected strength and ductility of the current BVS and point the way to thinner resorbable scaffolds in the future.

structural transformation | ductility | poly (L-lactide) | coronary heart disease | microdiffraction

Cardiovascular disease (CVD) claims over 15 million lives per year—more lives than communicable, maternal, neonatal, and nutritional disorders combined and more than twice the number of deaths due to all cancers (1). Coronary heart disease (CHD), the narrowing of coronary arteries due to the deposition of plaque, accounts for nearly 50% of all CVD deaths (1). To restore blood flow, most patients receive minimally invasive balloon angioplasty followed by stent implantation (1 million in 2008 in the United States) (2). Stents are metal mesh tubes that are delivered to the target lesion while they are crimped onto a balloon. Once they are positioned at the lesion, inflation of the balloon compresses the plaque against the vessel wall and deploys the stent to provide support at the enlarged diameter after the balloon is deflated and withdrawn. Metal stents are permanent, and their stiffness prohibits vasomotion and dilation (3, 4). Further, they present a lifelong risk of late stent thrombosis (3–6). A new technology is poised to displace metal stents: bioresorbable vascular scaffolds (BVS), which have been deemed the "fourth revolution" in percutaneous coronary intervention (7, 8).

The goal of tissue scaffolds is to restore the healthy state of the tissue, rather than merely ameliorating the diseased state (9–11). Poly(L-lactide) (PLLA) was selected as the material for BVS because its semicrystalline structure gives it adequate radial strength [>300 mm Hg (12)], and it degrades into products that are metabolized by the human body (13–16). Clinically, bioresorption of PLLA vascular scaffolds occurs within 2–3 y, and the treated segment of the coronary artery is restored in terms of vasomotion and vasoresponse (17–19). Success of a BVS depends on its ability to withstand deformation during both crimping onto the balloon and deployment at the lesion and still have sufficient strength to hold the artery open for 6 mo or more. Achieving this with PLLA is remarkable in view of the literature, which describes PLLA as a brittle material with a fracture strain ranging from 5 to 13% at temperatures below 30 °C (20–22). Scaffold deployment in the arteries occurs in aqueous media, for which the scant literature reports a strain at break of PLLA less than 10% (23). The usual approaches to overcoming the tendency of PLLA to fracture, blending (24, 25) and copolymerization (26–28), are not acceptable for BVSs because they reduce the lifetime of the polymer in the body (28, 29). Therefore, the material (pure PLLA) at the heart of the first clinically approved vascular scaffold [European Conformity (CE Mark) in 2011 (4) and US Food and Drug Administration (FDA) approval in July 2016 (30)] is notorious for being brittle.

The processes for production and implantation for both stents and scaffolds appear superficially similar: tube formation, laser-cutting of the strut lattice, crimping, and deployment (8). However, the strain fields and their effect on material structure and properties are dramatically different. PLLA scaffolds (~150 μm thick) (8) are thicker than metal stents (~80 μm) (31) due to the lower stiffness and mechanical strength of polymers relative to metals. As a result, greater strains are encountered during crimping and deployment of polymeric scaffolds. For example, elongation at the outer bend (OB; Fig. 1*B*) of a U crest during crimping can be as high as 50% in the θ direction (Fig. S1). This solid-state deformation of the as-cut PLLA scaffold (Fig. 1*A*) is performed near its glass transition ($T_g \sim 60$–65 °C), where its properties depend strongly on temperature (22) and accurate, predictive models are not yet available. Furthermore, the effect of processing strain on the semicrystalline microstructure of a polymer is crucial for understanding its performance, but modeling deformation-induced morphology in semicrystalline polymers is a persistent challenge (32). Therefore, direct observations of changes in semicrystalline morphology caused by deformation are needed, and the

Significance

Bioresorbable vascular scaffolds (BVSs) are poised to replace permanent metal stents for the treatment of coronary heart disease (CHD), which claims over 7 million lives each year. BVSs support the artery for 6 mo but completely dissolve in 2 y, eliminating serious long-term complications. The first clinically approved BVS is made from a brittle material, poly (L-lactide) (PLLA), yet it does not fracture during crimping or deployment. We used X-ray microdiffraction to discover multiple, micron-scale morphologies in the crimped BVS, which confer ductility to PLLA and resist fracture upon deployment. Contrary to intuition, the crimping process enhances scaffold strength, a result that researchers should keep in mind when designing thinner scaffolds to make BVSs broadly applicable to CHD.

Author contributions: A.A., K.R., and J.A.K. designed research; A.A. and K.R. performed research; M.B.K., J.P.O., and J.A.K. contributed new reagents/analytic tools; A.A., K.R., and J.A.K. analyzed data; and A.A., K.R., and J.A.K. wrote the paper.

Conflict of interest statement: M.B.K. and J.P.O. are employees of Abbott Vascular. Funding for this research was provided by Abbott Vascular.

This article is a PNAS Direct Submission.

[1]A.A and K.R contributed equally to this work.

[2]To whom correspondence should be addressed. Email: jakornfield@cheme.caltech.edu.

This article contains supporting information online at www.pnas.org/lookup/suppl/doi:10.1073/pnas.1602311113/-/DCSupplemental.

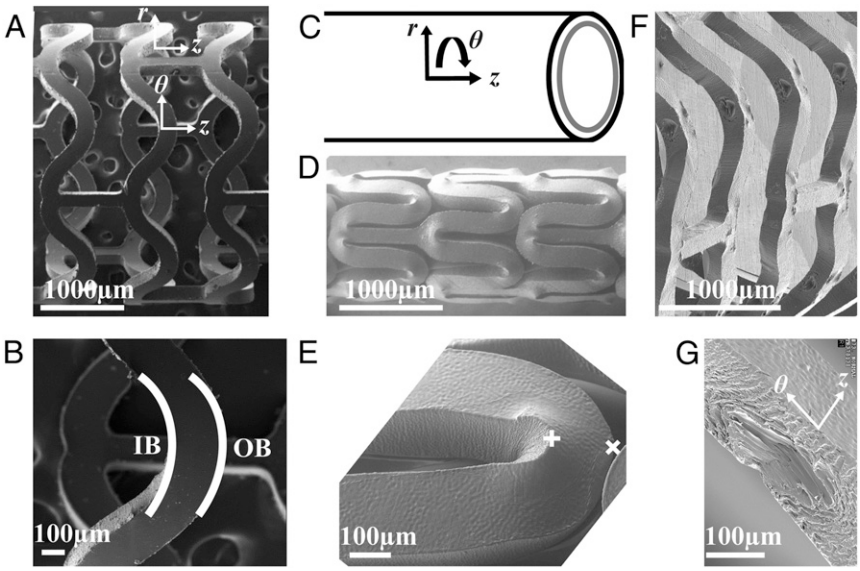

Fig. 1. SEMs of the subassemblies (as-cut, crimped, and deployed) of a PLLA vascular scaffold. The expanded tube is laser-cut to create an (*A*) as-cut scaffold. (*B*) The U crest of an as-cut scaffold indicating the IB and OB. (*C*) Cylindrical coordinate system for the scaffold. (*D*) Crimped scaffold. (*E*) A U crest of a crimped scaffold in *D*. (*F*) Deployed scaffold. (*G*) Diamond-shaped voids present in a deployed U crest.

inhomogeneous strain field imposed on the BVS during crimping demands investigation by a technique that offers micron-scale resolution. Recent advances in X-ray microdiffraction (33) meet this need and provide results that reveal the basis of the balance of ductility and strength that enables PLLA vascular scaffolds: crimping creates a multiplicity of materials from a single one—with strong and ductile regions arranged favorably for deployment.

Results

During the development of PLLA scaffolds, the relationship between the conditions used to produce the expanded tube, before laser cutting, and the properties of the resulting scaffold were investigated. An extruded PLLA preform was subjected to a biaxial elongation during tube expansion, and the relationship of hoop elongation and axial elongation (Table S1) to mechanical properties (Fig. S2) was measured. Surprisingly, group 5 (200% hoop and 200% axial elongation; Table S1), the most ductile tube (elongation at break >25% in both the hoop and axial directions; Fig. S2 *C* and *D*), did not perform well upon deployment [deployment diameter at which fracture began was only ∼3.6 mm (Fig. S2*F*) and had the largest number of fractured elements upon reaching that diameter, >40 per scaffold; Fig. S2*G*]. Similarly, the expanded tube with the second best mechanical properties (group 4, hoop elongation to break ∼15% and axial elongation to break ∼45%; Fig. S2 *C* and *D*) also fractured upon deployment (∼15 cracks per scaffold; Fig. S2*G*). Contrary to expectation, expanded tubes with inferior mechanical properties (groups 1–3; Table S1) gave superior structural integrity where it counts—upon deployment (fewer than five cracks per scaffold; Fig. S2*G*). To our knowledge, no explanation of this surprising finding has ever been offered.

To understand the success of BVS, the present study focuses on scaffolds produced with the tube expansion conditions that are used for current clinical BVS devices (group 3; Table S1). The

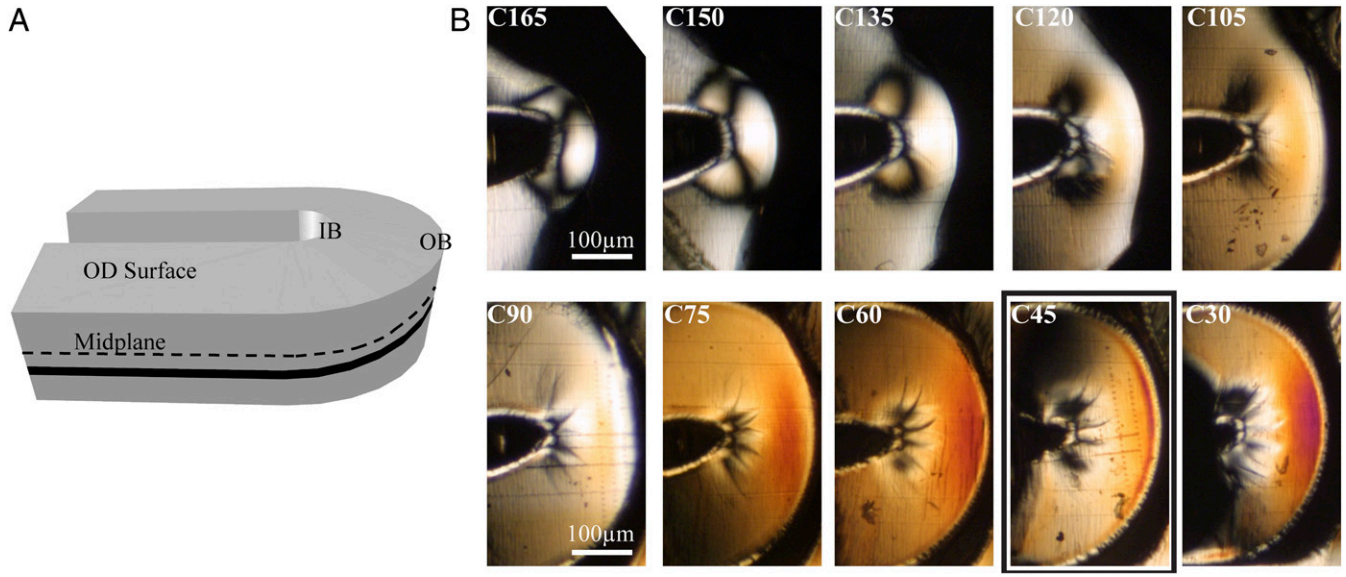

Fig. 2. Variation in birefringence through the thickness of a crimped PLLA vascular scaffold. (*A*) Schematic of a U crest (Fig. 1*E*) indicating the OD surface, the midplane (black dotted line), and the position of a particular section (black band). (*B*) Cropped polarized light micrographs of sequential 15-μm-thick microtomed sections from the OD to the ID of a crimped U crest. Sections are labeled with C to denote "crimped" and the approximate distance in microns from the inner diameter of the scaffold (i.e., C30 was closest to the scaffold's ID, and C165 was closest to its OD). A bold rectangle indicates the section analyzed in Fig. 3.

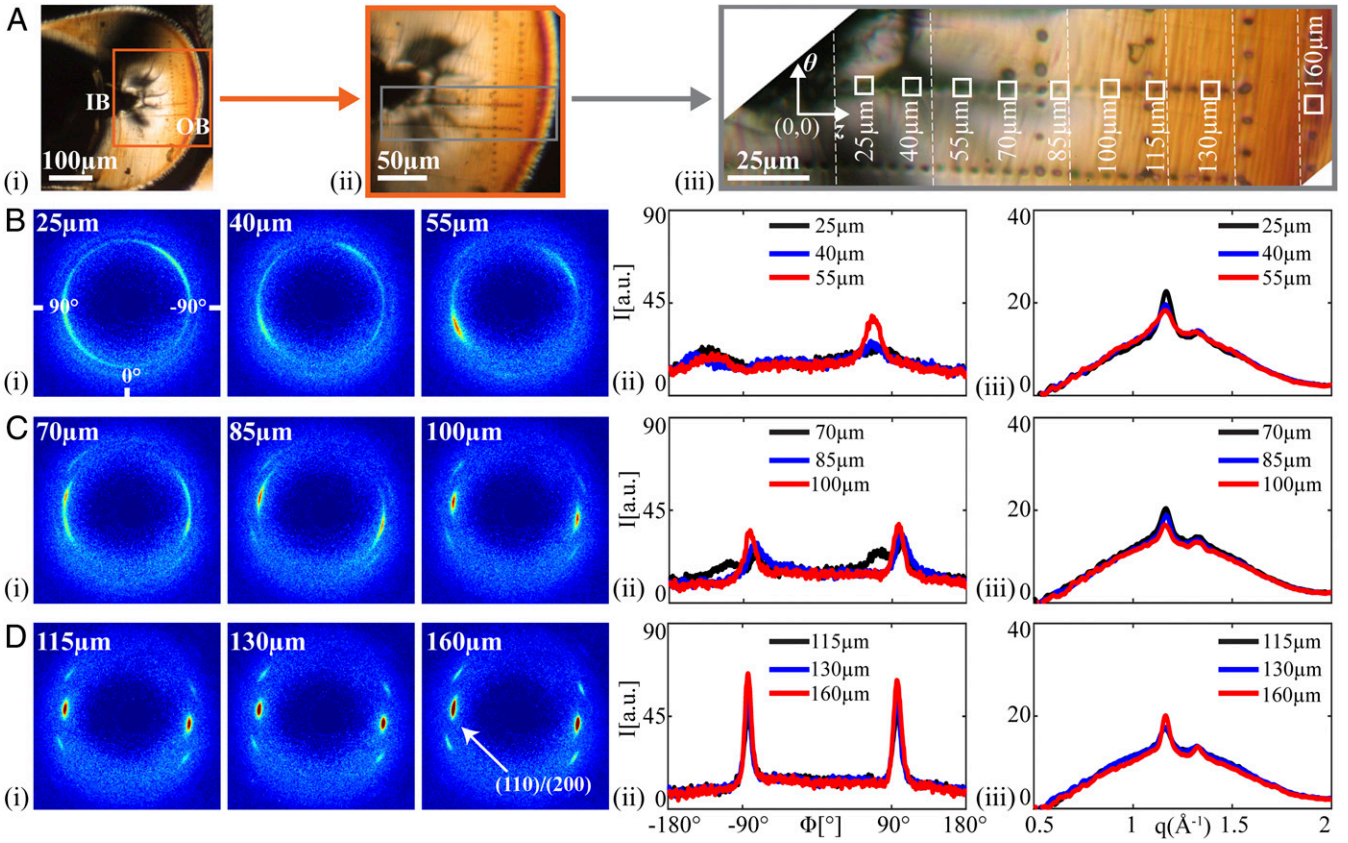

Fig. 3. Structural characterization of a crimped U section (C45, bold rectangle in Fig. 2*B*). (*A*) Polarized light micrographs of C45 with increasing magnification from *A*, *i*, to provide context relative to the IB and OB, to (*A*, *iii*) a composite image (vertical dotted lines mark transitions between images) that shows positions of microdiffraction acquisitions (marked using the X-ray beam). Squares correspond to patterns shown in *B*–*D*. Microdiffraction data acquired (*B*) close to the IB, (*C*) midway between the IB and OB, and (*D*) close to the OB: (*B*–*D*, *i*) X-ray microdiffraction patterns, (*B*–*D*, *ii*) azimuthal intensity distribution I(ϕ) at the (110)/(200) diffraction (identified in *D*, *i*, azimuthal coordinates in (*B*, *i*, averaged over $q \in 1.08$–1.24 Å^{-1}), and (*B*–*D*, *iii*) radial intensity distribution I(*q*) (azimuthally averaged).

resulting scaffolds afford a wide margin of safety for overdilation without fracture (to ∼3.8 mm with few cracks, approximately five per scaffold; Fig. S2 *F* and *G*). The apparent contradiction between ductility of the expanded tube and the performance during deployment motivates investigation of the structural changes that occur during crimping, which reduces the diameter of the scaffold from 3.5 mm in the as-cut form (Fig. 1*A*) to 1.7 mm in the crimped state (Fig. 1*D*). Scanning electron micrographs (SEM) of crimped scaffolds show that the deformation zones are localized to areas that are ∼100 μm across (compare Fig. 1 *B* and *E*). Compression along the θ direction (defined in Fig. 1 *C* and *G*) occurs at each inner bend (IB; Fig. 1*B*) causing material to bulge out of the (θ, *z*) plane (Fig. 1*E*). Thus, an elongation in the *r* direction occurs at each inner bend, which does not occur in metal stents (Fig. S3). At each outer bend (Fig. 1*B*), tension along the θ direction causes the scaffold to thin in the *r* direction. Upon deployment (Fig. 1*F*), the inner bend is placed under tension, but it does not fracture, despite the brittle character associated with PLLA. Instead, a diamond-shaped void forms (Fig. 1*G*) (34) in the scaffold, a feature not observed in metal stents (Fig. S3).

Although prior data showed that the formation of diamond-shaped voids correlates with successful deployment without fracture (Fig. S2 *G* and *H*), no explanation of this correlation has yet been offered. Unlike cracks, diamond-shaped voids are conical cavities at the inner bends of U, W, and Y crests (Fig. S4*A*) that do not rupture either the outer diameter (OD) or inner diameter (ID) surface. To understand the microstructural basis of this mechanism for yielding without failure, we use X-ray microdiffraction to gain a 3D view of the morphology created during crimping and deployment. In particular, we characterize structural transformations that occur in U crests, which permit estimates of the strain imposed during crimping (Fig. S1). Relative to the original 150-μm thickness of the as-cut scaffold (Fig. 1*A*), the bulge at each inner bend causes an increase in thickness to ∼180 μm (position + in Fig. 1*E*), and the tensile deformation at the outer bend causes a decrease in thickness to ∼110 μm (position × in Fig. 1*E*).

Resolution in the radial direction (*r*; Fig. 1*C*) is achieved by microtoming sections in the (θ, *z*) plane (Fig. 1 *A* and *G*). Moving from the OD to the ID of the scaffold (upper left to lower right in Fig. 2*B*), we observe a steady increase in the birefringence. A possible explanation for this trend is the gradient in both temperature and strain that is set up during tube expansion (35), before laser cutting. When hot PLLA comes into contact with a cooler outer mold, the material close to the outer diameter is quenched, which hinders crystallization near the OD. In addition, the tube expansion step imposes larger strains on material at the ID (∼400%) than at the OD (∼100%). Consequently, the material close to the ID has a greater driving force for oriented crystallization and a longer time to crystallize before vitrification, which may explain the observed gradient in birefringence.

A coarse-grain map of the distribution of orientation in the (θ, *z*) plane, obtained using polarized light microscopy, shows craze structures at the IB and strong orientation at the OB. In contrast to the gradient in the *r* direction (from one section to the next in Fig. 2*B*), gradients of birefringence in the plane of each section must have been created by the crimping process (Fig. 1*D*) because the expanded tube has uniform structure in the (θ, *z*) plane. The compressive forces that lead to bulge formation (Fig. 1*E*) cause plastic deformation and crazing at the IB (black lines emanating from the cusp of the inner bend in Fig. 2*B*) (36).

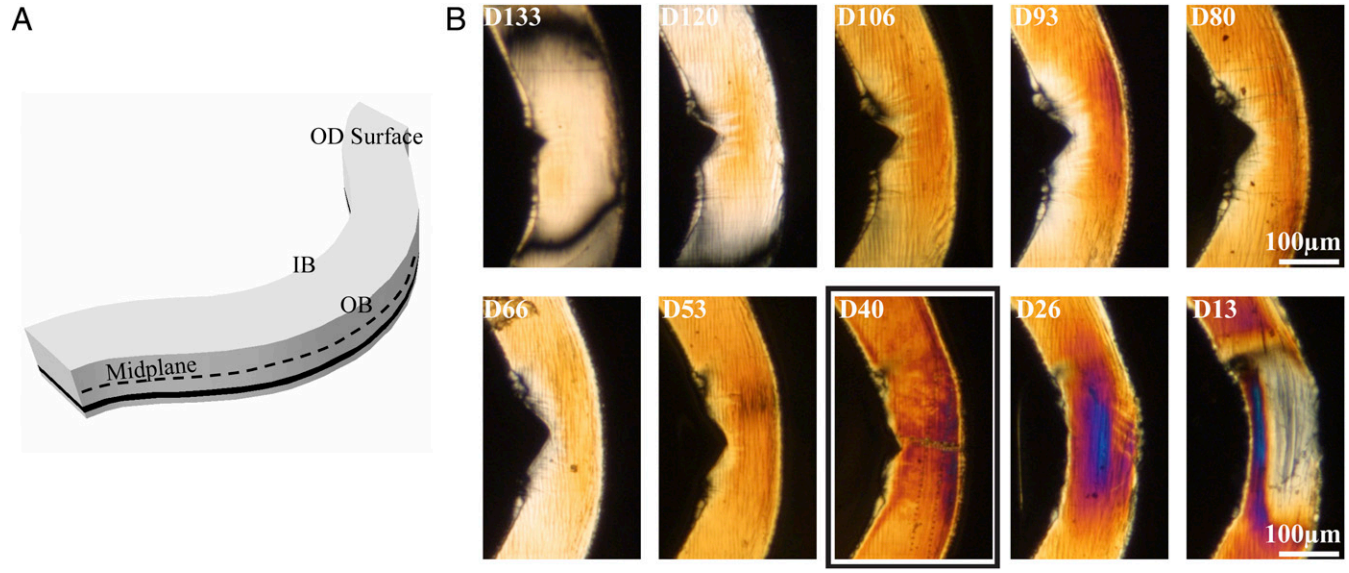

Fig. 4. Variation in birefringence through the thickness of a deployed PLLA vascular scaffold. (*A*) Schematic of a U crest (Fig. 1*G*) indicating the OD surface, the midplane (black dotted line), and the position of a particular section (black band). (*B*) Cropped polarized light micrographs of sequential 15-μm-thick microtomed sections from the OD to the ID of a deployed U crest. Sections are labeled with D to denote "deployed" and the approximate distance in microns from the inner diameter of the scaffold (i.e., D13 was closest to the ID of the scaffold, and D133 was closest to its OD). A bold rectangle indicates the section analyzed in Fig. 5.

Midway between the IB and the OB, there is a relatively uniform region (orange Michel–Levy color in Fig. 2*B*, C45). At the outer bend, the tensile forces in the θ direction during crimping result in strong orientation (burnt orange Michel–Levy color in Fig. 2*B*, C45). Of particular relevance to the formation of diamond-shaped voids, section C45 contains the deepest fissures at the IB; thus, we examine C45 using microdiffraction to probe the role of crimping in the formation of diamond-shaped voids and enhancing the tensile strength of the scaffold.

Resolution in the (θ, z) plane is achieved by translating the sample relative to the microdiffraction beam [beamline 2-ID-D of the Advanced Photon Source (APS), Argonne National Laboratory, 200-nm-diameter irradiated area], typically using 5-μm steps. The line of measurement points highlighted in Fig. 3*A*, *iii*, spans from the compression region at the IB to the tensile region at the OB. At the IB we observe striking, highly asymmetric diffraction patterns (Fig. 3*B*, *i*; 25–55 μm from the innermost edge) and complex azimuthal variation of (110)/(200) intensity (Fig. 3*B*, *ii*). We believe this is a result of the yielding that occurs under severe compression. Moving away from the IB (70–100 μm), the middle zone is characterized by progressively stronger orientation (Fig. 3*C*, *i*). Moving to the OB, the crystallites have their *c* axis strongly aligned parallel to the θ direction (Fig. 3*D*, *i*), giving a narrower azimuthal distribution (Fig. 3*D*, *ii*; ~10°, Fig. S5*G*). Despite its reputation for being brittle, the PLLA does not fracture under the tension at the OB during crimping; instead, the structure transforms to one with orientation parallel to the OB and, thus, gains tensile strength. The yielding and restructuring in the compact zone near the inner bend (0–85 μm; Fig. 3*B*) preserve the integrity of the rest of the material (100–160 μm; Fig. 3*D*) during crimping.

To mimic deployment of a scaffold in an artery, a crimped scaffold is immersed for two minutes in phosphate-buffered saline (PBS) at 37 °C and then radially expanded by inflation of a balloon. The radial sequence of sections (Fig. 4*B*) shows notches at the inner bend corresponding to the diamond-shaped void that forms upon deployment (Fig. 1 *F*–*G*): the notch is deepest near the midplane (D80 and D93; Fig. 4*B*). The birefringence in the deployed sections is higher than that seen in the crimped sections (compare Fig. 2*B* to Fig. 4*B*). Microdiffraction analysis was performed on section D40, similar to the *r* position of section C45 above.

The 2D scattering patterns are remarkably similar at all positions from IB to OB (Fig. 5 *B*–*D*, *i*). The intensity and azimuthal breadth of the (110)/(200) diffraction peaks (Fig. 5 *B*–*D*, *ii*) and the relative magnitude of the crystalline diffraction to the amorphous scattering (Fig. 5 *B*–*D*, *iii*) hardly vary along the path from IB to OB. In contrast to the dramatic variations in structure in the crimped state (Figs. 2 and 3 and Fig. S5), the deployed state is remarkably uniform (Figs. 4 and 5 and Fig. S6). During deployment, the IB is placed under tension, and a diamond-shaped void is observed. In the vicinity of the void, there is no evidence of fissures or yielding; there are no craze fibrils crossing the diamond-shaped void, nor any crazing near it. Deployment places the OB under compression, yet again there are no indications of yielding; the material at the OB retains the strong θ orientation (~10°; Fig. S6*E*) that was seen in the crimped state. Although the formation of diamond-shaped voids might at first appear to be a defect in the scaffold, the morphology in the deployed state suggests that the gentle separation of the surfaces of the diamond-shaped void allows the material to relax into a uniform, oriented structure, consistent with mechanical integrity and radial strength in the bulk (group 3, Fig. S2 *E*–*H*). Thus, the crazing and reorientation at the inner bend produced by crimping permits the uniformity and integrity of the deployed state, explaining the previously paradoxical observation that scaffolds with a high incidence of diamond-shaped voids resist fracture upon deployment (Fig. S2 *G*–*H*).

Conclusions

The structural integrity of BVSs is of paramount importance to their clinical success (37). Scaffolds must not fracture even if overdilated during implantation and must retain their strength for 6 mo (38) to support the occluded artery. The requirement of lasting strength is the compelling advantage of pure PLLA relative to more ductile PLLA blends or copolymers. The mechanical strength of BVSs is governed by their semicrystalline microstructure, which is determined by the complex interplay of thermal and strain histories imparted during tube expansion, crimping, and deployment. Processing conditions for tube expansion must be carefully selected because the resulting microstructure influences the response of PLLA upon crimping and deployment.

The fine spatial resolution of microdiffraction data at the deformation regions of interest shows that the multiplicity of morphologies created during crimping (Fig. 3) works in tandem to enable deployment without failure. Looking back at the crimped state (Fig. 2), it is noteworthy that the birefringence in the (θ, z)

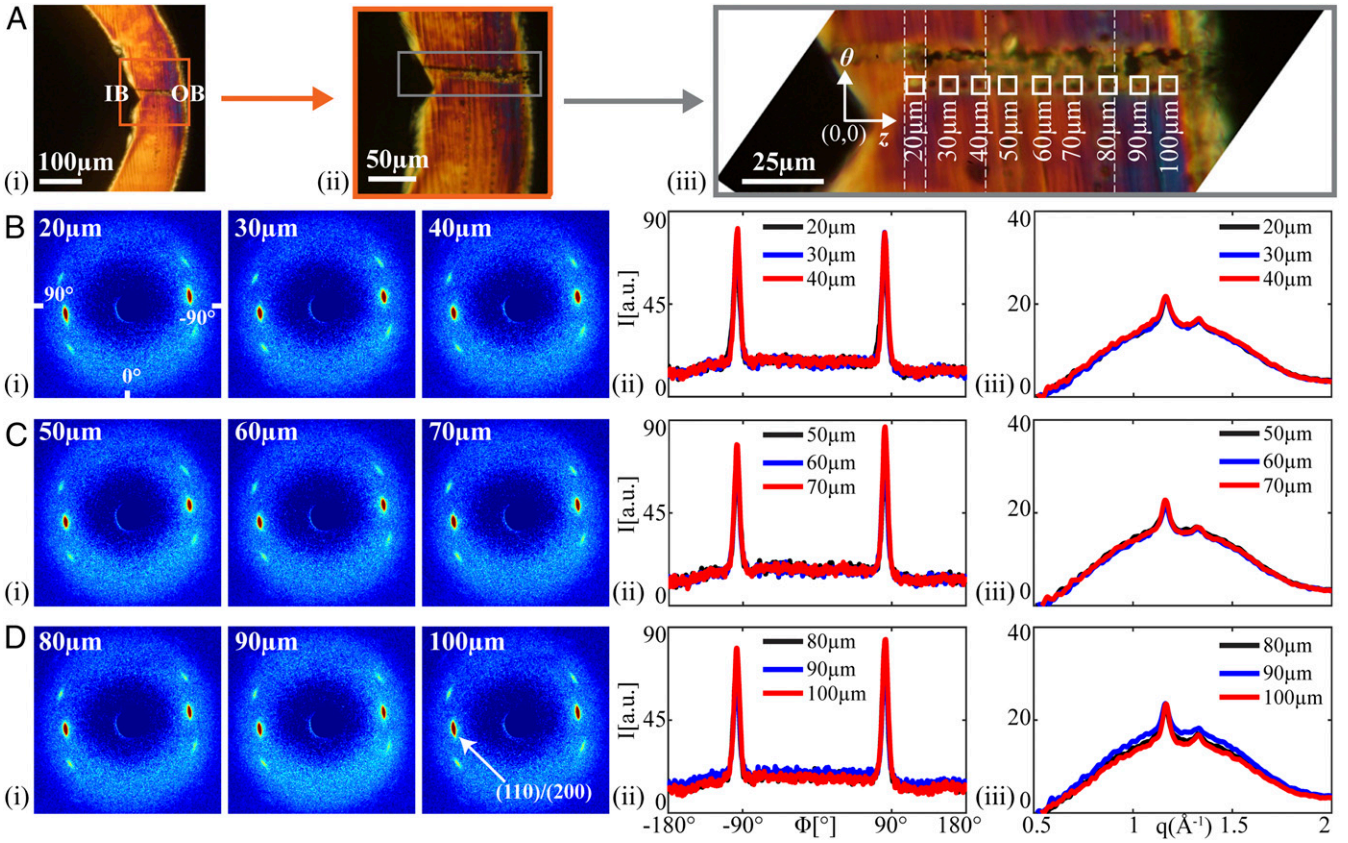

Fig. 5. Structural characterization of a deployed U section (D40; bold rectangle in Fig. 4*B*). (*A*) Polarized light micrographs of D40 with increasing magnification from *A*, *i*, to provide context relative to the IB and OB, to (*A*, *iii*) a composite image (vertical dotted lines mark transitions between images) that shows positions of microdiffraction acquisitions (marked using the X-ray beam). Squares correspond to patterns shown in *B*–*D*. Microdiffraction data acquired (*B*) close to the IB, (*C*) midway between the IB and OB, and (*D*) close to the OB: (*i*) X-ray microdiffraction patterns, (*ii*) azimuthal intensity distribution I(ϕ) at the (110)/(200) diffraction (identified in *D*, *i*, azimuthal coordinates in *B*, *i*, averaged over $q \in 1.08$–1.24 Å^{-1}), and (*iii*) radial intensity distribution I(*q*) (azimuthally averaged).

plane was low at the IB, consistent with chains being oriented out of plane (along *r*). In semicrystalline polymers, a graceful separation of surfaces is possible when the chain axis is tangential to the surface (no chains need to be extended or broken). Thus, the reorganization of the semicrystalline structure during crimping sets the stage for formation of the diamond-shaped voids (Fig. 1*G*) that permit deployment with relatively little tensile stress at the IB. In turn, the low tensile stress at the IB during deployment protects the OB from high compressive stresses. The results presented in this report caution against focusing solely on the tube expansion step in the design of thinner scaffolds. Contrary to intuition, scaffolds gain strength from the crimping process because it can impart a morphology that confers ductility to a nominally brittle material.

Vascular scaffolds are designed to be as thin as possible to minimize disruption of blood flow through coronary arteries. Despite the clinical success of 150-μm-thick scaffolds, clinicians seek even thinner BVS to treat smaller and more complex arterial lesions. PLLA preforms can be expanded to a thickness comparable to that of permanent stents (~80 μm), but they must be strong enough to resists vessel spasms (~300 mm Hg) (12) to support the occluded artery. Concerns regarding faster degradation of thinner scaffolds are mitigated by the fact that there is negligible mass loss at 12 mo for current BVSs—twice the time required for supporting the artery (38). A thinner scaffold is expected to relieve the compression of the inner bend during crimping and reduce the out-of-plane strain; thus, the present results suggest that thinner scaffolds will have proportionately smaller diamond-shaped voids. To bring a thinner scaffold to the clinic, its hoop strength must match that of current BVSs, requiring the material to have greater strength; the present findings point to the crimping step as a key process that can increase strength in thinner BVSs, extending their benefits to a broader patient population.

Materials and Methods

Preparation of Vascular Scaffolds. The scaffolds used for this study were produced by Abbott Vascular through a multistep procedure: pure poly(L-lactide) with a T_g between 60 and 65 °C was extruded into tubes; the extruded tubes were expanded from an outer diameter of ~1.5 mm to an outer diameter of 3.5 mm and wall thickness of 150 μm using stretch blow molding; the scaffolds were formed from the expanded tube by laser-cutting the desired pattern of axial struts and azimuthal rings (Fig. S4*A*); and the scaffolds were coated with a 2- to 2.5-μm layer of amorphous poly(D,L-lactide), similar to the clinical coating except for the omission of the antiproliferative drug, crimped over a delivery balloon, and sterilized with electron beam radiation. From the same batch of crimped scaffolds used for this study, some of the scaffolds were deployed in vitro using balloon inflation in a bath of saline at physiological temperature (37 °C). Thus, the crimped and deployed scaffolds came from the same lot of PLLA and were processed under the same specifications, on the same equipment, and by the same operators. The scaffolds were stored in a −80 °C freezer to preserve material properties (i.e., prevent aging) and were taken out for sectioning. A detailed description of the scaffold manufacturing process may be found in the patent literature (39, 40).

Microtomed Sections of Crimped and Deployed Subassemblies. Consecutive sections in the (θ, *z*) plane, each ~15 μm thick, were provided by Abbott Vascular. The sections were obtained by carefully controlling the orientation of the scaffold of interest (crimped or deployed) during embedding in a clear colorless plastic methylmethacrylate-based embedding medium (Technovit 7100; Electron Microscopy Sciences) using a 120-min cure at 25 °C. The size of the specimen usually included two to three consecutive U crests (outlined in Fig. S4*A*), which were oriented in the embedding material such that the U crests were in a plane near the surface where the block face could be cut. The embedded sample was glued to the microtome mounting post oriented with the *r* direction of the

sample parallel to the post axis. When placed in the microtome, the post was rotated to orient the *z* axis of the sample parallel to the cutting direction. Sections 15 μm thick were cut using a glass knife at −75 °C on a PowerTome XL Ultra-Microtome. The block face was cut, and excess embedding material was removed until the plane of the U crests was first exposed. Starting with the first section that contained scaffold material, consecutive sections were carefully retained and labeled in sequence order until the sections no longer contained scaffold material. A representative section from a crimped sample (Fig. S4*B*) shows consecutive U crests in embedding medium.

Scanning Electron Microscopy of As-Cut, Crimped, and Deployed Vascular Scaffolds. The PLLA scaffolds were mounted on SEM sample stubs using carbon tape and then sputter coated with gold to improve conductivity during image acquisition. Images were acquired using a Zeiss 1550 VP Field Emission SEM at California Institute of Technology and a Hitachi S-4800 Field Emission Microscope at Abbott Vascular.

X-Ray Microdiffraction Measurements on 15-μm-Thick Scaffold Sections. The hard X-ray Scanning Microprobe (HXRSM) at beamline 2-ID-D of the APS at the Argonne National Laboratory was used to acquire the microdiffraction data. The HXRSM combines microfocusing capabilities with X-ray sensitivity to measure crystallographic strain and the ability to penetrate several microns through a specimen. The HXRSM uses radiation from the high-brilliance source generated by an electron beam of 7 GeV in the APS storage ring and a 3.3-cm-period undulator. The X-ray microprobe radiation has an energy in the range of 6–20 keV. For the present experiments, X-rays with energy of 10.1 keV ($\lambda = 1.227$ Å) were used. A combination of an Si(111) monochromator and a white beam slit located 43.5 m upstream of the zone plate can achieve a minimum spot size of 0.15 μm. For our studies, a 0.2-μm beam spot size was used. Further details of the beamline optics can be found in the literature (41). A Mar165 CCD area detector at 2-ID-D was used to acquire 2D scattering patterns. The samples were mounted on an aluminum holder. Using a CeO_2 standard, the *q* range was calibrated, and the sample-to-detector distance was measured to be 119.923 mm. A detailed description of the X-ray analysis can be found in Figs. S7–S12.

Polarized Light Microscopy of Crimped and Deployed Scaffold Sections. Polarized light micrographs were acquired at 4×, 10×, or 32× magnification through crossed linear polarizers using a Zeiss Universal microscope equipped with a Canon EOS DS30 camera. Image composites at 32× magnification were stitched together using Adobe Photoshop, Illustrator, and Microsoft Powerpoint. Dotted white lines have been used to indicate the position where two different images have been stitched together.

ACKNOWLEDGMENTS. This research used resources of the Advanced Photon Source (APS), a US Department of Energy (DOE) Office of Science User Facility operated for the DOE Office of Science by Argonne National Laboratory under Contract DE-AC02-06CH11357. We thank Dr. Zhonghou Cai at APS for his assistance in collecting x-ray microdiffraction data, and Mr. Troy P. Carter (Abbott Vascular) for sectioning the scaffolds. We appreciate the assistance of Dr. Nobumichi Tamura at the Advanced Light Source, Lawrence Berkeley National Laboratories, for proof-of-concept x-ray microdiffraction measurements. The Advanced Light Source is supported by the Director, Office of Science, Office of Basic Energy Sciences, of the US Department of Energy under Contract DE-AC02-05CH1123. Funding for this research was provided by Abbot Vascular.

1. Nichols M, Townsend N, Scarborough P, Rayner M (2014) Cardiovascular disease in Europe 2014: Epidemiological update. *Eur Heart J* 35(42):2950–2959.
2. Epstein AJ, Polsky D, Yang F, Yang L, Groeneveld PW (2011) Coronary revascularization trends in the United States, 2001-2008. *JAMA* 305(17):1769–1776.
3. Ormiston JA, et al. (2008) A bioabsorbable everolimus-eluting coronary stent system for patients with single de-novo coronary artery lesions (ABSORB): A prospective open-label trial. *Lancet* 371(9616):899–907.
4. Wiebe J, Nef HM, Hamm CW (2014) Current status of bioresorbable scaffolds in the treatment of coronary artery disease. *J Am Coll Cardiol* 64(23):2541–2551.
5. Stettler C, et al. (2007) Outcomes associated with drug-eluting and bare-metal stents: A collaborative network meta-analysis. *Lancet* 370(9591):937–948.
6. Ong DS, Jang I-K (2015) Causes, assessment, and treatment of stent thrombosis–intravascular imaging insights. *Nat Rev Cardiol* 12(6):325–336.
7. Onuma Y, Serruys PW (2011) Bioresorbable scaffold: The advent of a new era in percutaneous coronary and peripheral revascularization? *Circulation* 123(7):779–797.
8. Oberhauser JP, Hossainy S, Rapoza RJ (2009) Design principles and performance of bioresorbable polymeric vascular scaffolds. *EuroIntervention* 5(Suppl F):F15–F22.
9. Derby B (2012) Printing and prototyping of tissues and scaffolds. *Science* 338(6109):921–926.
10. Tibbitt MW, Rodell CB, Burdick JA, Anseth KS (2015) Progress in material design for biomedical applications. *Proc Natl Acad Sci USA* 112(47):14444–14451.
11. Langer R, Tirrell DA (2004) Designing materials for biology and medicine. *Nature* 428(6982):487–492.
12. Agrawal CM, Haas KF, Leopold DA, Clark HG (1992) Evaluation of poly(L-lactic acid) as a material for intravascular polymeric stents. *Biomaterials* 13(3):176–182.
13. Burdick JA, Frankel D, Dernell WS, Anseth KS (2003) An initial investigation of photocurable three-dimensional lactic acid based scaffolds in a critical-sized cranial defect. *Biomaterials* 24(9):1613–1620.
14. Kang S-K, et al. (2016) Bioresorbable silicon electronic sensors for the brain. *Nature* 530(7588):71–76.
15. Rolland JP, et al. (2005) Direct fabrication and harvesting of monodisperse, shape-specific nanobiomaterials. *J Am Chem Soc* 127(28):10096–10100.
16. Farokhzad OC, et al. (2006) Targeted nanoparticle-aptamer bioconjugates for cancer chemotherapy in vivo. *Proc Natl Acad Sci USA* 103(16):6315–6320.
17. Ormiston JA, et al. (2012) First serial assessment at 6 months and 2 years of the second generation of absorb everolimus-eluting bioresorbable vascular scaffold: A multi-imaging modality study. *Circ Cardiovasc Interv* 5(5):620–632.
18. Sarno G, et al. (2012) Morphological and functional evaluation of the bioresorption of the bioresorbable everolimus-eluting vascular scaffold using IVUS, echogenicity and vasomotion testing at two year follow-up: A patient level insight into the ABSORB A clinical trial. *Int J Cardiovasc Imaging* 28(1):51–58.
19. Serruys PW, et al. (2016) A polylactide bioresorbable scaffold eluting everolimus for treatment of coronary stenosis: 5-year follow-up. *J Am Coll Cardiol* 67(7):766–776.
20. Grijpma DW, Pennings AJ (1994) (Co) polymers of L-lactide, 2. Mechanical properties. *Macromol Chem Phys* 195(5):1649–1663.
21. Xu H, et al. (2012) Formation of shish-kebabs in injection-molded poly(L-lactic acid) by application of an intense flow field. *ACS Appl Mater Interfaces* 4(12):6774–6784.
22. Nakafuku C, Takehisa SY (2004) Glass transition and mechanical properties of PLLA and PDLLA-PGA copolymer blends. *J Appl Polym Sci* 93(5):2164–2173.
23. Renouf-Glauser AC, Rose J, Farrar DF, Cameron RE (2005) The effect of crystallinity on the deformation mechanism and bulk mechanical properties of PLLA. *Biomaterials* 26(29):5771–5782.
24. Hu Y, Rogunova M, Topolkaraev V, Hiltner A, Baer E (2003) Aging of poly(lactide)/poly(ethylene glycol) blends. Part 1. Poly(lactide) with low stereoregularity. *Polymer (Guildf)* 44(19):5701–5710.
25. Broz ME, VanderHart DL, Washburn NR (2003) Structure and mechanical properties of poly(D,L-lactic acid)/poly(ε -caprolactone) blends. *Biomaterials* 24(23):4181–4190.
26. Rathi S, et al. (2011) Toughening semicrystalline poly(lactic acid) by morphology alteration. *Polymer (Guildf)* 52(19):4184–4188.
27. Grijpma DW, Pennings AJ (1994) (Co) polymers of L-lactide, 1. Synthesis, thermal properties and hydrolytic degradation. *Macromol Chem Phys* 195(5):1633–1647.
28. Huang MH, Li S, Vert M (2004) Synthesis and degradation of PLA-PCL-PLA triblock copolymer prepared by successive polymerization of ε-caprolactone and DL-lactide. *Polymer (Guildf)* 45(26):8675–8681.
29. Li S (1999) Hydrolytic degradation characteristics of aliphatic polyesters derived from lactic and glycolic acids. *J Biomed Mater Res* 48(3):342–353.
30. Rizik DG, Padaliya BB (2016) Early U.S. experience following FDA approval of the ABBOTT vascular bioresorbable vascular scaffold: Optimal deployment technique using high resolution coronary artery imaging. *J Interv Cardiol*, 10.1111/joic.12329.
31. Pache J, et al. (2003) Intracoronary stenting and angiographic results: Strut thickness effect on restenosis outcome (ISAR-STEREO-2) trial. *J Am Coll Cardiol* 41(8):1283–1288.
32. Bergström JS, Hayman D (2016) An overview of mechanical properties and material modeling of polylactide (PLA) for medical applications. *Ann Biomed Eng* 44(2):330–340.
33. Ice GE, Budai JD, Pang JWL (2011) The race to x-ray microbeam and nanobeam science. *Science* 334(6060):1234–1239.
34. Radu MD, Onuma Y, Rapoza RJ, Diletti R, Serruys PW (2012) In vivo visualisation by three-dimensional optical coherence tomography of stress crazing of a bioresorbable vascular scaffold implanted for treatment of human coronary stenosis. *EuroIntervention* 7(12):1461–1463.
35. Martin C, et al. (1997) Investigation of the variation in orientation and crystallinity in poly(ethylene terephthalate) containers using microfocus X-ray diffraction. *J Synchrotron Radiat* 4(Pt 4):223–227.
36. Donald AM, Kramer EJ (1982) The competition between shear deformation and crazing in glassy polymers. *J Mater Sci* 17(7):1871–1879.
37. Iqbal J, et al. (2014) Bioresorbable scaffolds: Rationale, current status, challenges, and future. *Eur Heart J* 35(12):765–776.
38. Kossuth MB, Perkins LEL, Rapoza RJ (2016) Design principles of bioresorbable polymeric scaffolds. *Interv Cardiol Clin* 5(3):349–355.
39. Schmitz KP, et al. (2009) Polymeric, degradable drug-eluting stents and coatings. US Patent Appl 13/057,974.
40. Wang Y (2014) Bioabsorbable scaffolds made from composites. US Patent Appl 13/107,643.
41. Cai Z, et al. (2000) Performance of a high-resolution x-ray microprobe at the Advanced Photon Source. *AIP Conf Proc* 521(30):31–34.
42. Aou K, Kang S, Hsu SL (2005) Morphological study on thermal shrinkage and dimensional stability associated with oriented poly (lactic acid). *Macromolecules* 38(18):7730–7735.
43. Glauser T, et al. (2015) Controlling crystalline morphology of a bioabsorbable stent. US Patent Appl 12/559,400.
44. Galvin E (2014) Characterisation of the performance of an absorbable magnesium stent by experimental and numerical analysis. PhD thesis (Dublin City University, Dublin, Ireland).
45. Basalus MW, et al. (2012) Recent insights from scanning electron microscopic assessment of durable polymer-coated drug-eluting stents. *Interv Cardiol* 4(6):661–674.
46. Ding N, Pacetti S, Tang F, Gada M, Roorda W (2009) XIENCE V (TM) stent design and rationale. *J Interv Cardiol* 22(s1):S18–S27.